University of Birmingham
Research at Birmingham

Self-assembled calcium pyrophosphate nanostructures for targeted molecular delivery

Bassett, David C; Robinson, Thomas E; Hill, Reghan J; Grover, Liam M; Barralet, Jake E

DOI:
10.1016/j.bioadv.2022.213086

License:
Creative Commons: Attribution (CC BY)

Document Version
Publisher's PDF, also known as Version of record

Citation for published version (Harvard):
Bassett, DC, Robinson, TE, Hill, RJ, Grover, LM & Barralet, JE 2022, 'Self-assembled calcium pyrophosphate nanostructures for targeted molecular delivery', *Biomaterials advances*, vol. 140, 213086.
https://doi.org/10.1016/j.bioadv.2022.213086

Link to publication on Research at Birmingham portal

General rights
Unless a licence is specified above, all rights (including copyright and moral rights) in this document are retained by the authors and/or the copyright holders. The express permission of the copyright holder must be obtained for any use of this material other than for purposes permitted by law.

•Users may freely distribute the URL that is used to identify this publication.
•Users may download and/or print one copy of the publication from the University of Birmingham research portal for the purpose of private study or non-commercial research.
•User may use extracts from the document in line with the concept of 'fair dealing' under the Copyright, Designs and Patents Act 1988 (?)
•Users may not further distribute the material nor use it for the purposes of commercial gain.

Where a licence is displayed above, please note the terms and conditions of the licence govern your use of this document.

When citing, please reference the published version.

Take down policy
While the University of Birmingham exercises care and attention in making items available there are rare occasions when an item has been uploaded in error or has been deemed to be commercially or otherwise sensitive.

If you believe that this is the case for this document, please contact UBIRA@lists.bham.ac.uk providing details and we will remove access to the work immediately and investigate.

Download date: 20. Apr. 2024

140 (2022) 213086

Contents lists available at ScienceDirect

Biomaterials Advances

journal homepage: www.journals.elsevier.com/materials-science-and-engineering-c

Self-assembled calcium pyrophosphate nanostructures for targeted molecular delivery

David C. Bassett [a], Thomas E. Robinson [a], Reghan J. Hill [b], Liam M. Grover [a,*], Jake E. Barralet [c,*]

[a] *Healthcare Technologies Institute, School of Chemical Engineering, University of Birmingham, UK*
[b] *Department of Chemical Engineering, McGill University, Canada*
[c] *Department of Dentistry, McGill University, Canada*

ARTICLE INFO

Keywords:
Calcium pyrophosphate
Nanofibre microsphere
Nanotube
Self-assembly
Drug delivery

ABSTRACT

Nanostructured, inorganic microspheres have many industrial applications, including catalysis, electronics, and particularly drug delivery, with several advantages over their organic counterparts. However, many current production methods require high energy input, use of harmful chemicals, and extensive processing. Here, the self-assembly of calcium pyrophosphate into nanofibre microspheres is reported. This process takes place at ambient temperature, with no energy input, and only salt water as a by-product. The formation of these materials is examined, as is the formation of nanotubes when the system is agitated, from initial precipitate to crystallisation. A mechanism of formation is proposed, whereby the nanofibre intermediates are formed as the system moves from kinetically favoured spheres to thermodynamically stable plates, with a corresponding increase in aspect ratio. The functionality of the nanofibre microspheres as targeted enteric drug delivery vehicles is then demonstrated *in vitro* and *in vivo*, showing that the microspheres can pass through the stomach while protecting the activity of a model protein, then release their payload in intestinal conditions.

1. Introduction

Calcium phosphates are widely studied and utilised for biomedical applications, primarily for dental and orthopaedic treatments [1–4]. This is because the principal mineral in both bones and teeth is hydroxyapatite $Ca_{10}(PO_4)_6(OH)_2$, [5–8] and thus several calcium phosphate materials have been investigated to replace, repair and restore these tissues. Calcium phosphates have also been investigated as drug delivery vehicles, owing to their favourable biocompatibility, biodegradability, and material properties [9,10]. In addition to orthophosphate, the single tetrahedral ion, calcium has a strong affinity for many other phosphate based oxyanions, including the two-membered, P-O-P linked pyrophosphate [11,12], the so-called hexametaphosphate [13,14], and other longer chain polyphosphates [15,16]. Unlike calcium orthophosphates, which often crystallise rapidly, calcium polyphosphates can exist as stable amorphous, glassy materials [17,18]. Indeed, it is thought that the ability to *co*-localise high concentrations of calcium and phosphate without crystal formation is one of the key roles of polyphosphates *in vivo* [19].

Pyrophosphate, consisting of two phosphate tetrahedra linked by an oxygen atom, is the smallest of the polyphosphates. It is a well-known inhibitor of calcium orthophosphate crystallisation, both *in vitro* and *in vivo* [19–21], however calcium pyrophosphate itself can form crystals [22,23]. Biomedically this phenomenon is most well-known in conditions of calcium pyrophosphate deposition disease (CPPD), more commonly known as pseudo-gout, a form of arthritis. In this disease crystalline calcium pyrophosphate dihydrate crystals form deleteriously in articulating joints causing pain and inflammation [24,25].

Nanostructured particulate materials and nanotubes have recently attracted substantial interest for application in a broad range of industrial sectors. Their high specific surface area and tortuous pore networks provide them with significant benefits as drug release vehicles [26], catalyst supports [27], chromatography adsorbents [28] and in electronic applications [29]. Currently, nanoporous microspheres are synthesized by indirect routes that require the use of, and therefore subsequent removal of, templating surfactants [30], porogens [31] or emulsion formers [32]. Inorganic nanotubes, meanwhile, are currently grown *via* sulphurisation of reactive oxides and halides, precursor decomposition, templated growth, pyrolysis and direct vapour phase synthesis, and more recently *via* hydrothermal, sol-gel, intercalation–exfoliation and sonochemical reactions [33]. The complexity of processing and the necessity for the use of environmentally harmful

---

* Corresponding authors.
E-mail addresses: Grover@bham.ac.uk (L.M. Grover), jake.barralet@mcgill.ca (J.E. Barralet).

https://doi.org/10.1016/j.bioadv.2022.213086
Received 27 May 2022; Received in revised form 20 July 2022; Accepted 15 August 2022

chemicals, high temperatures or costly catalysts currently limits widespread industrial, and especially medical, application.

Targeted oral delivery to the intestine is advantageous for both intestinal diseases, such as inflammatory bowel disease, and convenient delivery of pharmaceuticals, such as proteins, that are unstable in the stomach [34]. Oral administration is attractive due to ease of administration, patient compliance and cost effectiveness, compared to rectal or parenteral administration [35]. The key goals of such delivery vehicles are to protect the high-value therapeutic from gastric enzymes and low pH of the stomach environment, followed by release of the intact cargo in the intestine. This is most usually achieved by utilising a pH responsive system, either as a coating or bulk material, which is dense and impenetrable in the low pH of the stomach, but swells to release the therapeutic in the intestine [34,36–38]. Other strategies include vehicle degradation by enzymes only present in the intestine, and time-dependent release, though this can be difficult to achieve because of the large variation in gastrointestinal transit time between individuals [34,38]. The vast majority of these systems are polymer based, though a small number are inorganic, such as silica particles [38]. Inorganic systems are particularly advantageous because of their high chemical stability, as well as their low reactivity and tolerance within the digestive tract. However, as discussed above, creating inorganic particles structured at the nanoscale usually requires complex processing and harsh chemicals.

In this manuscript the self-assembly of calcium and pyrophosphate are examined. Fascinating nanostructures of the metastable intermediates formed in both static and agitated systems are revealed and characterised, to elucidate possible mechanisms of formation. The great potential of the formed nanofibre microspheres, which are created from only calcium and pyrophosphate at ambient temperature, as a targeted oral drug delivery excipient is then explored.

2. Materials and methods

2.1. Materials

Aqueous solutions were prepared using HPLC-grade water, 18.2 MΩ resistance (Millipore, Billerica, MA, USA). All chemicals of reagent grade quality were purchased from Sigma Aldrich (Oakville, ON, Canada) and used without further purification.

2.2. Nanostructured intermediate preparation

An initial amorphous precipitate was obtained by pouring 300 mM $CaCl_2$ into an equal volume of 150 mM $Na_4P_2O_7$, with both solutions adjusted to pH 7 with HCl and NaOH. To form nanofibre microspheres, the mixture was left static for around 30 min, then the microspheres were recovered *via* filtration through a vacuum filter, washed 3 times with double distilled water and 3 times with pure ethanol, then dried under vacuum at 25 °C. To instead form nanotubes, 1 mL of the initial mixture was immediately sealed in a 1.5 mL Eppendorf, inserted in a dental amalgamator (SDI Ultramat 2, SDI Ltd., Bayswater, Australia) and shaken at a frequency of 75 Hz and an amplitude of 5 mm for up to 20 min.

2.3. Electron microscopy

Growth of the microspheres and nanotubes was observed using scanning electron microscopy (FE-SEM, Hitachi S-4700, Japan, accelerating voltage 2 kV) and transmission electron microscopy (TEM, Philips Technai 12, Eindhoven, Netherlands, accelerating voltage 120 kV). Aliquots of the reaction mixture were taken at various times after initial mixing and immersed in excess ethanol to arrest the reaction. Samples were then deposited directly onto circular glass coverslips (diameter 12 mm) or 200 μm Ni TEM grids with carbon support films and allowed to dry in air. Glass coverslips were mounted on aluminium Cambridge stubs and sputter coated with Au/Pd prior to FE-SEM analysis. Calcium pyrophosphate particles were adhered to the surface of an aluminium stub using carbon tape. Particle cross sections made using a focused ion beam system (FB-2000A, Hitachi, Tokyo, Japan). After milling, the samples were imaged using FE-SEM.

2.4. X-ray diffraction

X-ray diffraction was performed on microspheres and nanotubes before and after crystallisation. A Philips powder X-ray diffractometer (Model PW 1710) was used with Cu Kα X-rays at a step size of 0.02° and collection time of 1 s across a 2θ range of 6–60°. Diffraction patterns were processed using X'Pert High Score (Version 2.0) software with reference to Powder Diffraction File database (Version 4+ 2005) of the International Centre for Diffraction Data (Newton Square, PA).

2.5. pH and ion concentration tracking

The pH of the reaction was monitored ($n = 4$) using a pH/ion meter (Oakton Instruments, Vernon Hills, IL, USA) connected to a micro pH combination electrode (Microelectrodes Inc. Bedford, NH, USA) and data logging software (CyberComm Pro 2.4.2). The pH electrode was calibrated using pH 4.00, pH 7.00 and pH 10.00 Fisher standard buffer solutions (SB101B, SB107B, SB115B, Fisher Scientific Company, Ottawa, ON, Canada). Calcium, sodium and pyrophosphate ions were monitored ($n = 6$) by ion chromatography (DX2500, Dionex, Sunnyvale, CA). At various timepoints 1 mL aliquots of the reaction liquor were taken and immediately centrifuged at 2000*g* for 20 s. A proportion of the supernatant was taken and diluted appropriately in DI water for analyses.

2.6. Surface area measurement

Specific surface area measurements were made using nitrogen adsorption apparatus, utilising the Brunauer–Emmet–Teller (BET) method to interpret the data (TriStar 3000, Micromeritics, Norcross, GA).

2.7. Gastrointestinal drug delivery model

The drug release properties of the nanofibre microspheres were determined *in vitro* using the physiologically based extraction test (PBET) [39], a model of the digestive tract using gastric (fed stomach, pH 4) and intestinal (pH 7) solutions. Nanofibre microspheres were loaded by suspending 100 mg of microspheres in 10 mL of a 10 mg mL^{-1}, pH 4 albumin or horse radish peroxidase (HRP) solution for 30 min. Following this immersion, the microspheres were washed thoroughly with distilled water and then vacuum filtered, and dried at 25 °C. Protein loading was quantified through thermogravimetric analysis (TA Instruments, Model SDT Q600, New Castle, DE). 10 mg of the loaded microspheres were placed in 10 mL of gastric solution at 37 °C, and agitated by bubbling nitrogen at 0.2 L min^{-1}. 100 μL aliquots were taken at 10 and 20 min, at which point the solution was altered to simulate the intestinal environment. Further aliquots were taken every 2 min for 10 min during this phase. The amount of albumin and HRP released was quantified through a bicinchoninic acid total protein assay (Thermo Scientific Pierce). HRP enzyme activity was qualitatively determined by comparing samples of enzyme released from the spheres during the PBET assay or an equivalent amount free enzyme that had been passed through the PBET assay. 0.8 mL samples were taken from the final PBET timepoint and incubated with 0.2 mL 3-amino-9-ethylcarbazole (AEC) buffer for 10 min at 37 °C. Optical adsorption was measured at 495 nm using a UV–Vis-NIR spectrophotometer (Cary 5000, Varian, Palo Alto, CA). Results were compared to and expressed as % activity of an equivalent amount of fresh HRP prepared in 100 mM phosphate buffered saline (PBS) buffer at pH 7.

2.8. *In vivo behaviour of microspheres*

To determine the effect of passage through the gastrointestinal tract on the microspheres, a suspension of microspheres was given to mice by gastric gavage. 6 male BALB/c mice (5–6 weeks old) were obtained from Charles River Laboratories (Saint-Constant, QC, Canada). A suspension containing 300 mg microspheres in 1 mL of glycerol was prepared. 0.1 mL of this suspension was administered by gastric gavage to each of the mice. Mice were sacrificed by CO_2 asphyxiation at 30, 60 and 90 min following gavage, after which the stomach and intestinal tract were removed for examination by light microscopy and SEM. All procedures were approved by the McGill University Animal Care Committee (UACC).

3. Results

3.1. *Calcium pyrophosphate nanostructure formation*

On mixing solutions containing calcium and pyrophosphate ions, a precipitate immediately formed, at a pH of 3.7 (Fig. 1A), which was subsequently shown to be X-ray amorphous (Fig. 2c). When left under quiescent or low shear conditions, this precipitate sedimented and rearranged into nanofibres, which self-assembled into microspheres, around 10 μm in diameter, over 30 min (Fig. 1B). Leaving this intermediate phase in solution caused densification of the precipitate, and the transition from amorphous nanofibre microspheres to a stable crystalline phase (Fig. 1C). If the calcium and pyrophosphate solutions were not adjusted to pH 7 prior to mixing, the amorphous precipitate did not form microspheres, and was instead stable in solution over long time periods. Interestingly if, following mixing of the calcium and pyrophosphate solutions, the resulting precipitate was agitated vigorously, the initial phase rearranged into nanotubes, with the macroscopic form of a thick blue-grey liquid (Fig. 1D). These tubes were around 10 μm in diameter with an aspect ratio of around 400. When left in solution, a similar densification of the precipitate was observed, and the nanotubes crystallised, however the timescale for this was drastically reduced; 15–20 min compared to several hours for the microspheres (Fig. 1E).

3.2. *Characterisation of nanofibre microspheres and nanotubes*

The structure of the nanofibre microsphere intermediate was then examined in more detail. Using a focussed ion beam to reveal a cross section of a microsphere showed that the nanofibre structure seen at the surface persisted homogeneously throughout the volume (Fig. 2B), with randomly oriented fibres creating a nanoporosity of 53 %, as measured by helium pyconometry (data not shown). When a microsphere was re-immersed in water, the stable crystalline phase was seen to erupt from the sphere surface, suggesting formation *via* densification and direct phase transition, rather than dissolution and reprecipitation (Fig. 2A). The crystal structure of both the nanofibre microspheres and nanotubes

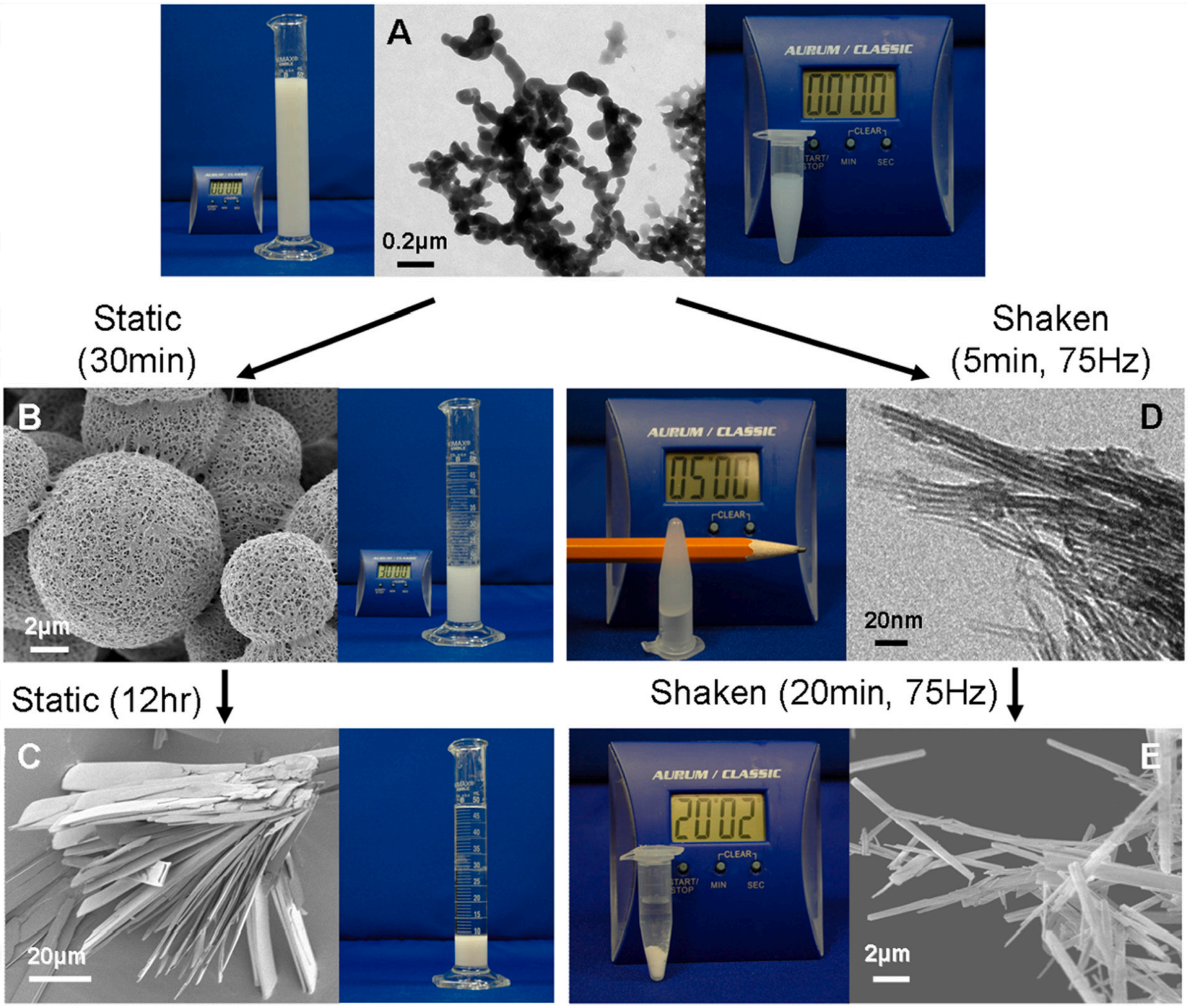

Fig. 1. Formation and change in structure of nanostructured calcium pyrophosphate. Precipitation of amorphous calcium pyrophosphate (A) was followed by the formation and crystallisation of nanofibrous microspheres under static conditions (B and C), and formation and crystallisation of nanotubes with vibration (D and E).

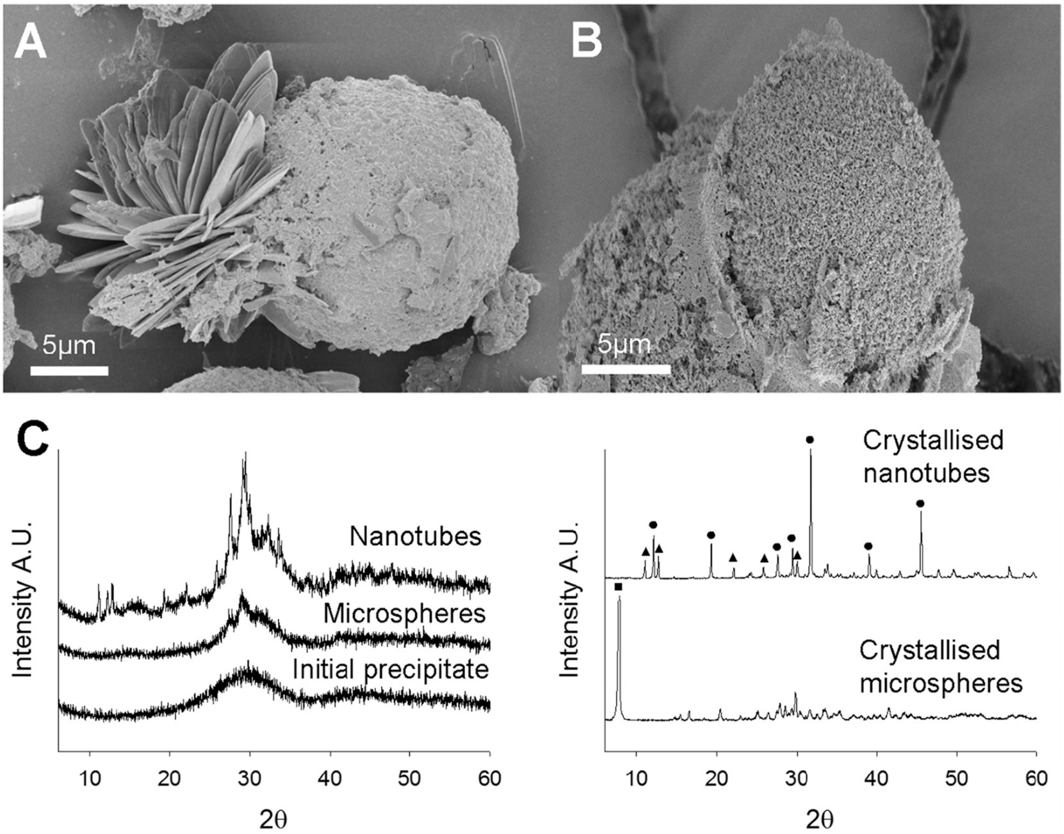

Fig. 2. Characterisation of nanostructured calcium pyrophosphate. Blade-like nanocrystals erupting from the surface of a microsphere on re-emersion in water (A). SEM image of a cross section through a microsphere, showing the homogeneity of the nanofibrous internal structure (B). X-ray diffraction patterns of the initial amorphous calcium pyrophosphate precipitate immediately after mixing (initial precipitate), nanofibrous microspheres and nanotubes (C left) and the products of aqueous crystallisation of nanotubes and microspheres (C right) (▲ triclinic calcium pyrophosphate dihydrate, ● monoclinic calcium pyrophosphate dihydrate, ■ β-calcium pyrophosphate tetrahydrate).

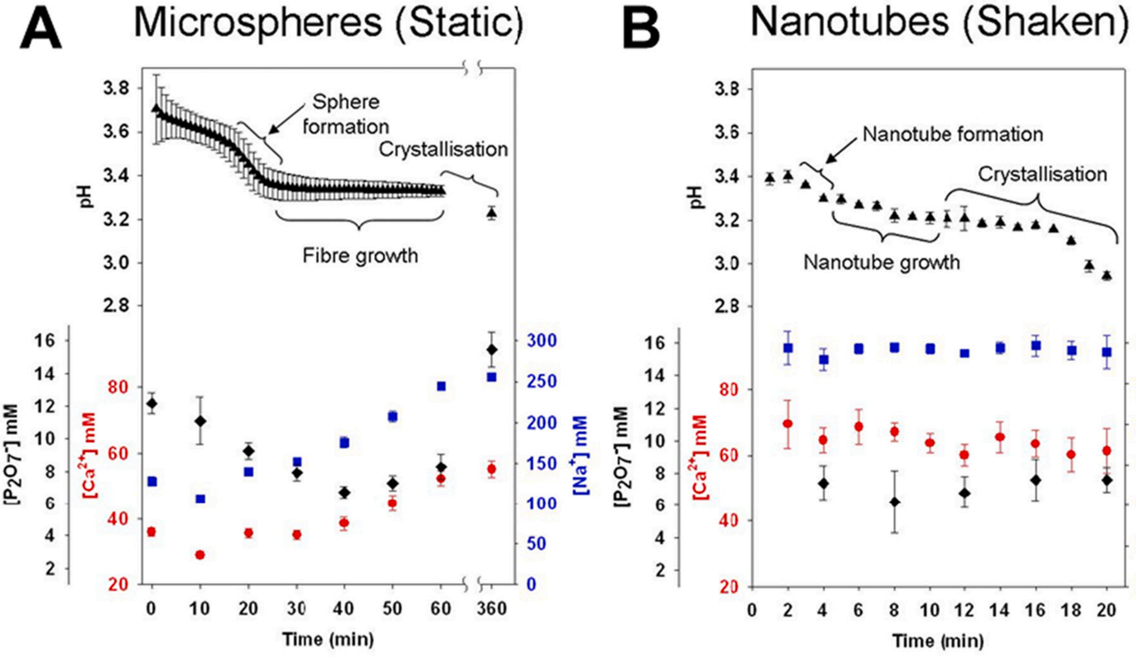

Fig. 3. Ionic concentration profiles during nanostructure formation. The change in pH (black triangles), calcium concentration (red circles), pyrophosphate concentration (black diamonds) and sodium concentration (blue squares) over time as the nanofibre microspheres in the static system (A) and nanotubes in the agitated system (B) form.

were studied *via* XRD (Fig. 2C). As expected, the initial precipitate was X-ray amorphous, as were both the nanofibre microspheres and nanotube intermediate phases, though the nanotubes appeared to have some crystallinity. As expected, both mature structures were crystalline, though critically were different phases. The crystallised nanotubes were formed of a mixture of monoclinic and triclinic calcium pyrophosphate dihydrate, while the stable phase emerging from the nanofibre microspheres was β- calcium pyrophosphate tetrahydrate.

The stark difference in nanostructure and phase between the nanofibre microspheres and nanotubes was investigated further by measuring the ion concentrations during formation. In the case of the microspheres, formed in quiescent conditions, the pH dropped immediately to 3.71 ± 0.16 following mixing, then dropping to a plateau at 3.33 ± 0.03 after 20–30 min, with a further drop later during crystal formation (Fig. 3A). The calcium concentration dropped rapidly from 150 to 35.9 ± 1.2 mM over the first minute, and continued to drop over the first 10 min, before rising over the next hour. The sodium concentration followed a similar pattern to the calcium. Similarly, the pyrophosphate dropped in the first minute from 75 to 12.2 ± 0.6 mM, however it continued to drop over the following 40 min, to a minimum of 6.7 ± 0.4 mM, before rising again.

During the formation of the nanotubes, under agitation, similar pH drops were observed, though over much shorter time frames, and to lower values; 3.39 ± 0.03 after 1 min, and a final pH of 2.94 ± 0.02 (Fig. 3B). However, the ionic concentration profiles were very different. The sodium concentration did not change, remaining constant at around 300 mM. The initial calcium concentration was higher at 69.6 ± 7.3 mM, but continuously to 61.4 ± 6.8 mM, while the initial pyrophosphate concentration was lower and remained constant at around 7.5 mM.

Over the same time frames as the ionic measurements, the nanostructures were imaged. In the static system, the initial precipitate which consisted of spheroidal agglomerates 40–200 nm in diameter which both grew to up to 600 nm in diameter and began to form fine mesh-like networks within 2 min (Fig. 4). However, within 5 min, these large agglomerates had disappeared, and the structure was finer and more uniform, consisting of spheroidal particles and short fibre networks between 15 and 20 nm in diameter. Between 5 and 15 min, coinciding with the minima in calcium and sodium concentration (Fig. 3A), the agglomerates self-assembled into microspheres, with a diameter of 5–15 μm. By 20 min, the larger spheroidal particles had mostly disappeared, giving way to a very refined network of nanofibers. These nanofibres appeared along with slightly larger individual spheroidal particles, which were perhaps feeding the growth of the fibres from their tips (Fig. 4, arrows). Beyond this the nanofibres continued to grow and the interconnectivity increased, as larger voids in the microspheres were filled leading to a more homogeneous system.

In the agitated system, the initial precipitate formed a suspension of amorphous nanotubes within 2 min (Fig. 5). These nanotubes formed disorganised bundles by 4 min, however on continuous agitation the nanotubes began to align, and at 9 min this alignment was total, with no disorganised bundles remaining. Over the next 5 min, the tubes densified *via* aqueous sintering to form nanofibres, which further densified through the transition to crystallinity.

3.3. Nanofibre microspheres as drug delivery systems

As they are prepared from safe, biocompatible materials and can be made at industrial scale, the nanofibre microspheres present a promising vehicle for drug delivery. The nanostructure of the microspheres imparts them with a large specific surface area of 125 $m^2 g^{-1}$, compared to 65 $m^2 g^{-1}$ for the initial precipitate and only 1.5 $m^2 g^{-1}$ for the final crystallised form. This presents the opportunity to adsorb large amounts of therapeutic for targeted delivery to a specific anatomic location. To test this, albumin and HRP were used as model proteins, and loaded into the particles, where both were readily adsorbed to the surface. The particles

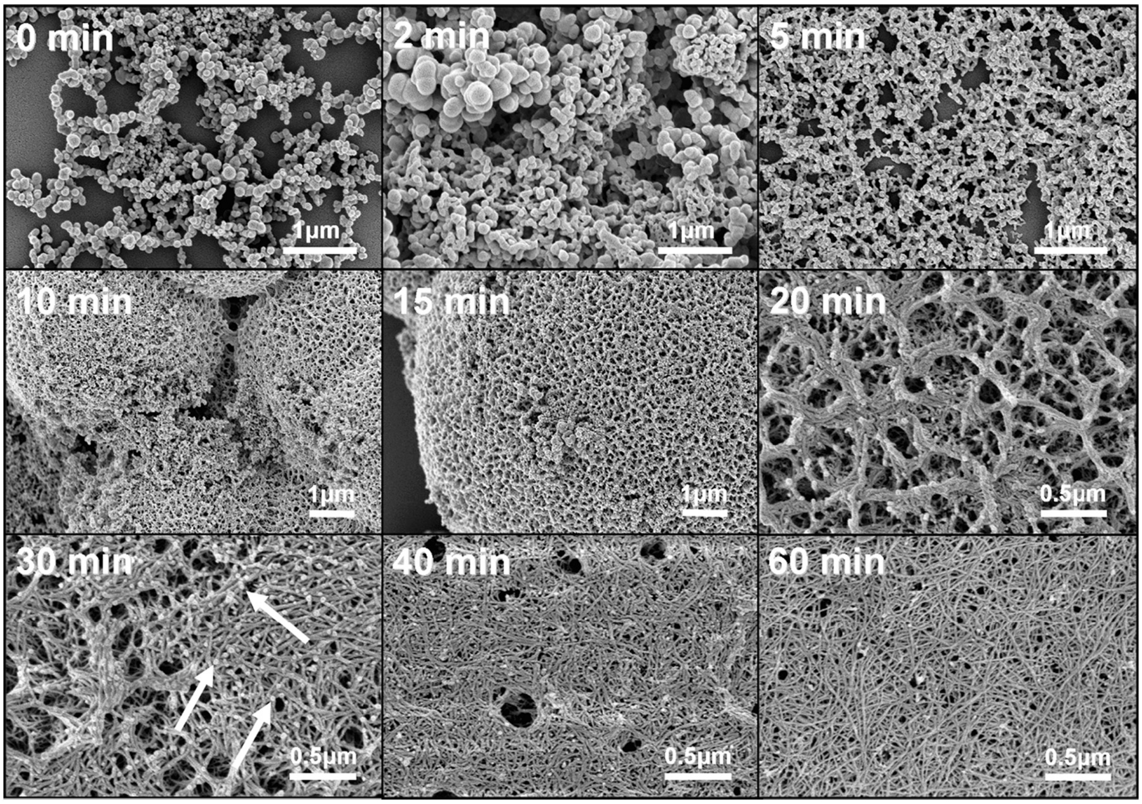

Fig. 4. The temporal structural development of nanofibre microspheres. SEM images showing the transition from disorganised initial precipitate (0 min) to microsphere formation (10 min), through the development of nanofibres (20 min) and their rearrangement into fine, homogeneous structures (60 min).

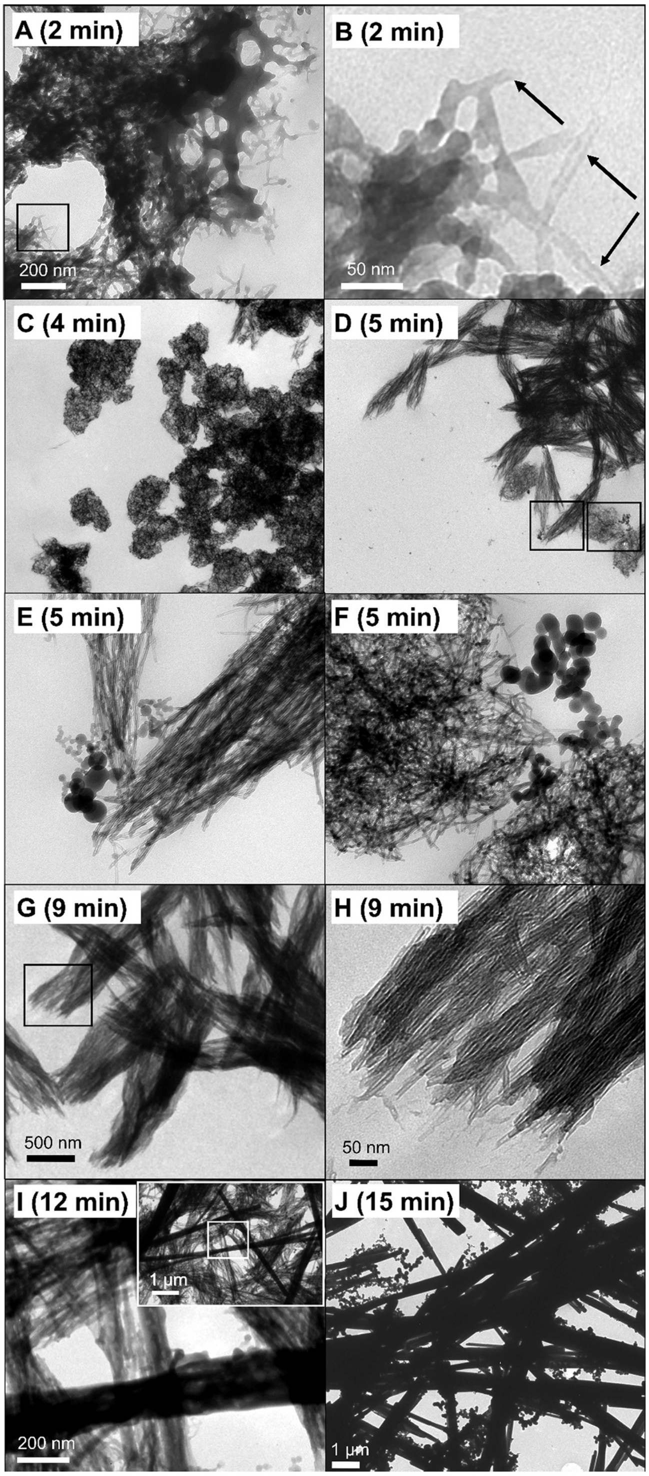

Fig. 5. The temporal structural development of nanofibre microspheres. TEM images showing the transition from disorganised, amorphous nanotubes (A, where B is a magnified image), which form bundles (C) then begin to align (E&F). This alignment is complete at 9 min (G, where H is a magnified image), after which the nanotubes densify through aqueous sintering to form fibres (I), and then crystallise (J).

were then placed in a model of the gastrointestinal tract, consisting of a fed stomach environment (pH 4) followed by an intestinal environment (pH 7).

Both proteins behaved similarly in the model (Fig. 6 A&B). A small amount of each was released in the stomach (15.2 % and 19.7 % of albumin and HRP, respectively) over 20 min. However, when in intestine conditions, the rate of release drastically increased, with a sustained release of around 7 % per minute for both proteins, over 10 min, until all the protein had been released. This was accompanied by rapid crystallisation of the microspheres. To assess the protection imbued to the proteins by the nanofibre microsphere carrier, the activity of free HRP was compared to that loaded into particles, following exposure to the stomach environment (Fig. 6C). The HRP protected by the microspheres was found to be over 15 % higher in activity than the free HRP.

Finally, an initial assessment of the *in vivo* behaviour of the nanofibre microspheres was undertaken. A preparation of the microspheres was administered to mice *via* oral gavage, and the contents of the stomach and intestines examined at various time points. All recovered microspheres appeared in tact, and many remained in the stomach for up to 90 min (Fig. 6C). Microspheres also passed the stomach, and were found in the intestine; up to 9 cm along by 30 min, 15 cm by 60 min, and 25 cm by 90 min.

4. Discussion

Creation of nanostructured particles usually requires a templating agent, which must later be removed, harsh chemicals that are environmentally hazardous and unsafe in the body, and/or extensive processing, making these materials unsuitable for industrial scale manufacture of biocompatible nanostructures. However, the large specific surface area of such materials is highly desirable for drug delivery, in order to adsorb large quantities of therapeutics into them, protect their payload *in vivo*, and then provide sustained release at the target site. Additionally, the use of nanostructures such as particles and tubes to template other materials is widely used, and so the ability to produce such templates easily from a soluble and non-toxic material will contribute to the further development of this technique. The ability to produce nanostructures safely at scale is also critical in the emerging field of nanoarchitectonics [40]. This study reports the first purely inorganic self-assembling system in which the reagents themselves, calcium and pyrophosphate, form nanostructured microparticles. The key advantage to this is that no purification is required, and all materials are safe for use *in vivo*. Further, this process uses relatively cheap starting materials, has only brine as the by-product, requires little processing and occurs at ambient temperature, making it a highly attractive route to manufacture of nanostructures at industrial scale.

It is hypothesised that the initially formed precipitate is composed of an amalgamation of ionic clusters. Intriguingly, the cation:anion ratio $\frac{Ca+\frac{Na}{2}}{P}$, calculated from the ionic profiling in Fig. 3, for the initial precipitate in this system is around 1.6, similar to that of Posner's clusters, 1.5 [41]. This could indicate the formation of a similar cluster, where one pyrophosphate ion takes the place of two orthophosphate (Fig. 7, 2–5 min). This data also suggests that the initial precipitate contains high quantities of sodium ions, a phenomena that has also been shown to occur in initial Posner's clusters when then initial reaction liquor contains high sodium concentration [42]. These models also suggest that sodium replaces the peripheral, rather than central, calcium ions in these clusters. The ionic profiles in this study (Fig. 3) show the Ca:Na ratio increasing as the reaction progresses, and it is postulated that this is because as the clusters aggregate and move towards crystallisation, there are fewer peripheral positions for the sodium to occupy.

Another consideration is the protonation state of the pyrophosphate ions in solution. At pH 7, the initial solution would be expected to contain approximately 3 % $P_2O_7^{4-}$, 87 % $HP_2O_7^{3-}$ and 10 % $H_2P_2O_7^{2-}$ [43]. The immediate drop in pH from the pure solutions at pH 7 to the precipitation mixture at 3.7 (Fig. 3) in the quiescent system may thus be attributed to preferential association of calcium and pyrophosphate, and the subsequent release of the associated protons into solution. In the agitated system, the pH drops immediately to 3.4, which does not happen in the static system until around 20 min, the point at which

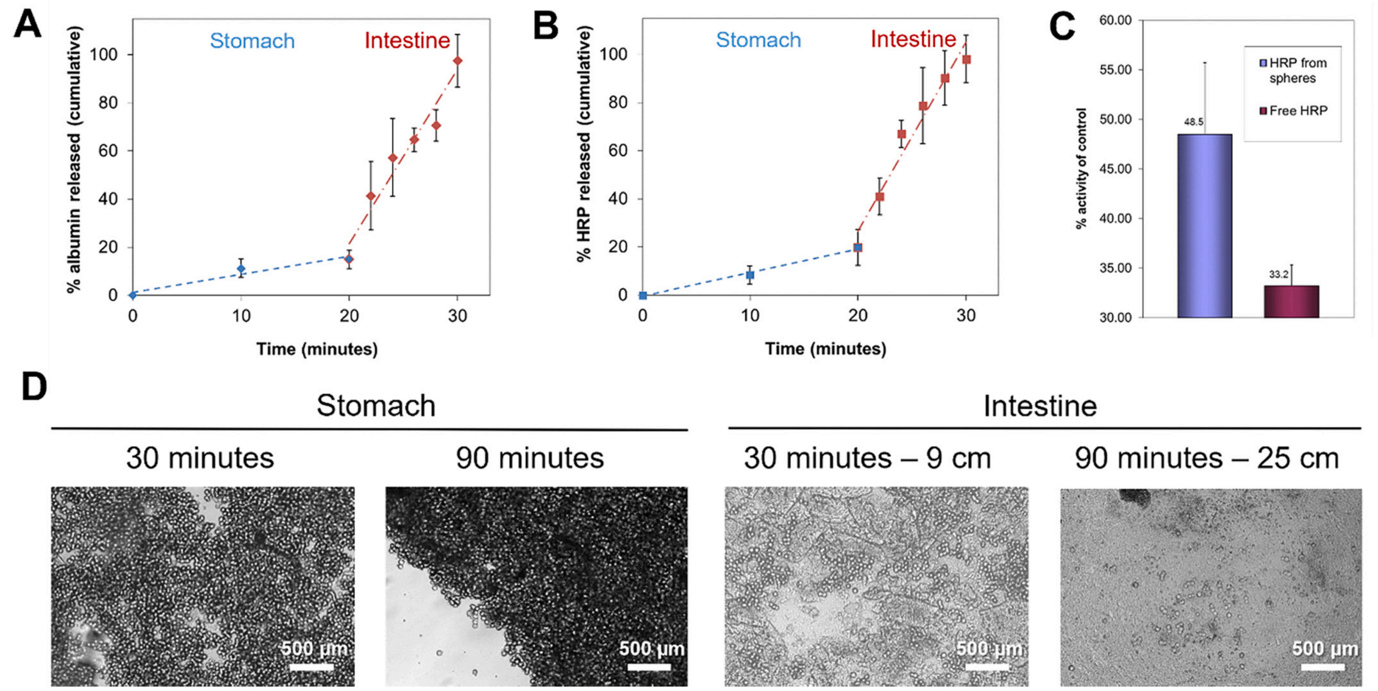

Fig. 6. Nanofibre microspheres as drug delivery systems. The release profiles of albumin (A) and HRP (B) in an *in vitro* model of the gastrointestinal tract. The activity of HRP, either free or protected by the microspheres, following exposure to stomach conditions (C). Images of the microspheres recovered from the stomach and intestines of mice following oral administration (D).

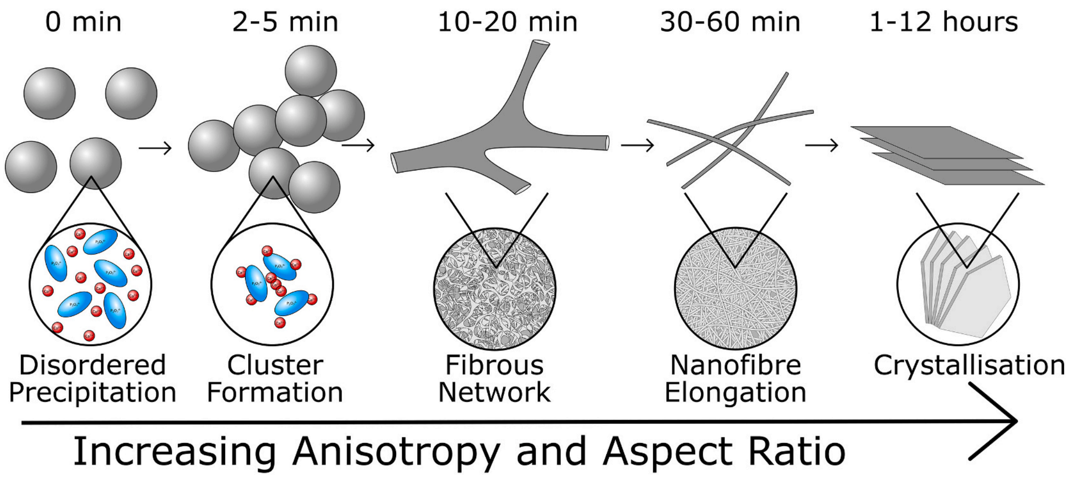

Fig. 7. Schematic of the proposed reaction mechanism in the static system. Ions of calcium and pyrophosphate immediately precipitate on contact, forming spheres as the most kinetically favourable structure. Within 5 min, the ions rearrange to form clusters with short range order which, along with incorporation of water, introduce anisotropy into the nanostructure, leading the spheres to form chains. As this reaction progresses over the next 20 min, clusters aggregate together, cations are expelled and water is incorporated, increasing the nanoscale anisotropy and networks of spheres merge to become branched networks, which form microscale spheres. This process continues, and the fibres become thinner and longer, with an ever-increasing aspect ratio, until they crystallise into mineral plates, over the course of hours.

fibres form. This is interesting because, in a computational study of Posner's clusters, it was shown that the initial aggregates were spherical where the phosphate species were protonated, and needle like where the phosphate was entirely deprotonated [42]. It may therefore be that the structures formed in the agitated system, anisotropic tubes (Fig. 5), occur at least in part because the agitation accelerates the deprotonation of the pyrophosphate though increased interaction frequency, leading to the larger immediate drop in pH, and the faster transition to needle-like structures.

In the absence of agitation, the precipitate initially forms spheroidal particles, the largest on the order of 100 nm in diameter (Fig. 4). This suggests that the ions in this immediate precipitate are randomly arranged, and the lack of order leads to a spherical morphology. As the precipitate matures, the spheres align to form branched networks (at 5 min), which subsequently transform into fibres (20 min) that get progressively thinner (30–60 min), prior to crystallisation as β-calcium pyrophosphate dihydrate, a plate-like mineral. This suggests that the initial regular spheres develop a degree of anisotropy, resulting in chain formation and the development of structures with increasing aspect ratio over time. Indeed, this indicates that the process represents the precipitate transforming from the most kinetically favourable formation (regular spheres) to the most thermodynamically stable (crystal) form, with a fascinating array of intermediate structures.

This progression from regular spheres to structures with ever increasing aspect ratio suggests the initial precipitate quickly becomes anisotropic. Formation of similar networks from spherical precipitates, albeit an order of magnitude smaller, have recently been observed [41,44], and it has been suggested that the prenucleation clusters, for example Posner's clusters or calcium triphosphate, arrange to form the unit cell of the final mineral, in this case octacalcium phosphate and hydroxyapatite, and that this structure is conserved throughout the reaction. The final mineral in this study, β-calcium pyrophosphate tetrahydrate, forms in plates bounded by a layer of water [45], a clearly anisotropic structure. It is thus proposed that the initial, spherical precipitate reorganises into an anisotropic structure similar to the unit cell of the final mineral product. This anisotropy, which may be increased further by the expulsion of cations and incorporation of water into the structure, causes the spheres to form branched chains, rather than coalescing uniformly, which then reorganise into fibres and finally into mineral plates (Fig. 7). The aspect ratio of the structures continuously increases as the reaction progresses and the anisotropic structures reorganise themselves. The nanofibres themselves forming microspheres may be due to convection currents in the reaction vessel, driven by the chemical gradients present while the reaction progresses, which act to converge the fibres into spheres of a certain size, rather than forming a single, integrated network.

The initial drop in the concentrations of all species up to around 10 min reaction time, and an accompanying small drop in pH, may be attributed to the continued formation of precipitation clusters, though the vast majority of ions form clusters almost immediately (Fig. 3A). However, this is concurrent with the formed clusters rearranging into their preferred anisotropic arrangement, and then forming nanofibres which begin to arrange into microspheres (Fig. 4). At around 10 min both calcium and sodium are released into solution, as the stoichiometry of the nanofibre microspheres moves from its initial, Posner cluster like cation:anion ratio of 1.5, towards the thermodynamically stable crystal structure with a lower ratio of 1. The drop in the pH at this point may suggest further deprotonation of the pyrophosphate species; indeed, in the final mineral the pyrophosphate is entirely deprotonated. At 40 min, the pH stabilises, however both cationic species (predominantly sodium) and pyrophosphate continue to be released back into solution. This could be due to the ever-decreasing specific surface area, allowing fewer ions which are not fully incorporated into the structures to be loosely bound at the interface; or because the nanofibre material is inherently more soluble, which may be further increased by the decreasing pH; or a combination of the two. After several hours, the material has crystalised, with a measured cation:anion ratio of 0.97, close to the theoretical value of 1 for β-calcium pyrophosphate dihydrate. It should also be noted that the apparent sodium substitution decreases over the course of the reaction, as the precipitate moves from loose clustering to crystal formation.

The nanotube structures formed when mechanical energy is applied to the system may be explained similarly to the quiescent system, but with key differences. The increased mechanical energy means that the ions interact with each other much more frequently, and thus structures are formed more quickly. This is evident as rod like structures, not seen in the quiescent system until 5–10 min, and are clear only at around 30 min (Fig. 4), are evident in only 2 min, and clearly visible after 9 min (Fig. 5). Both the increased mechanical energy present, which may break down loosely bound structures, and the increased rate of reaction, may lead to an alternative cluster formation, or even a bypassing of the cluster formation and rearrangement phase, going directly to an anisotropic tube phase which grow rapidly as ions collide with it at an increased rate. The increased anisotropy may also explain the alignment of the tubes prior to crystallisation, as the forces that cause stacking of the unit cells within tubes also attract the outside of tubes to each other, causing alignment.

This would explain both the formation of nanotubes, rather than nanofibres, as well as the difference in the final mineral formed if this was the preferred arrangement of this alternative unit cell. The fact that the final crystallised material is a mixture of multiple mineral phases (monoclinic and triclinic calcium pyrophosphate dihydrate) may imply that more than one anisotropic cluster formed, which then grew into a nanotube before it could reach its most thermodynamically preferably arrangement. Indeed, both experimental data and quantum modelling suggest that the tetrahydrate (formed in the static system) is the most thermodynamically stable at the low pH and ambient temperature used here [22,46]. The dihydrates, here formed in the agitated system, are more favourable at higher temperatures, and indeed some heating does occur in the agitated system (50–60 °C), though further studies are needed to understand the interplay between agitation and heating.

Nanostructured materials have a range of practical applications, many arising from their high specific surface area. The advantages of this system, chiefly the simple, low energy manufacturing route and the need for only two, non-harmful reagents, make it attractive for large scale processing from both a cost and environmental point of view. In targeted drug delivery, the vast majority of vehicles are based on polymers, however inorganic materials are advantageous because of their high chemical and mechanical stability, ease of functionalisation, and tuneable release properties [47,48]. The production of porous, inorganic microparticles usually involves the use of surfactants, solvents, porogens and/or templating agents [47–49], which require extensive post-processing to remove. Further, microparticle production often requires complex and expensive processing steps, such as emulsification, spray drying, freeze drying, and microfluidics [50]. Both the process itself, and the chemicals involved, may deactivate or destroy sensitive therapeutics, particularly high-value biologics such as proteins and mRNA [51,52]. In contrast, the system presented here produces only calcium pyrophosphate, which is FDA approved [53], and salt water as a by-product and requires no external energy inputs. To demonstrate the potential of calcium pyrophosphate nanofibre microspheres to act as enteric drug delivery vehicles for sensitive cargoes, initial experiments demonstrating effective delivery of two model proteins were performed *in vitro*. Both proteins were readily adsorbed to the particles through physical interactions, most likely hydrogen bonding and ionic interactions, which are strengthened by the highly negative charge density at the surface throughout the pH range of interest [54]. When placed in conditions simulating the stomach (Fig. 5A&B, pH 4), low amounts of the protein were released, suggesting the microspheres are able to transport proteins to the lower gastrointestinal tract. Once in the higher pH conditions of the intestines however (Fig. 5A&B, pH 7), the microspheres rapidly crystallised with a drastic reduction in surface area and subsequent release of nearly all the protein cargo over 10 min (Fig. 8). In addition to releasing in the intestines, a key role of an enteric drug delivery vehicle is to protect the therapeutic from the harsh, acidic environment of the stomach, for example to preserve the activity of an enzyme. By way of demonstration, it was shown that by loading HRP into the spheres, the activity of the enzyme could be maintained more effectively while passing through the stomach, than if the protein was free (Fig. 5C). An increase of 15 % was achieved in this study, however this may be increased with some optimisation of the system, for example ensuring most of the protein is within the interior of the sphere. In any case, as biological therapeutics can cost billions of pounds per kilogram [55], any improvement in activity retention using a cheap biomaterial is economically beneficial. Finally, the fate of the microspheres as they passed through the gastrointestinal tract was examined *in vivo* (Fig. 5D). The microspheres were found not to have been broken down by either the pH or enzymes present in the stomach, and could successfully pass through to the intestines to deliver their payload.

5. Conclusions

Mixing solutions of calcium and pyrophosphate immediately forms a regular spherical precipitate, which when left static form branched

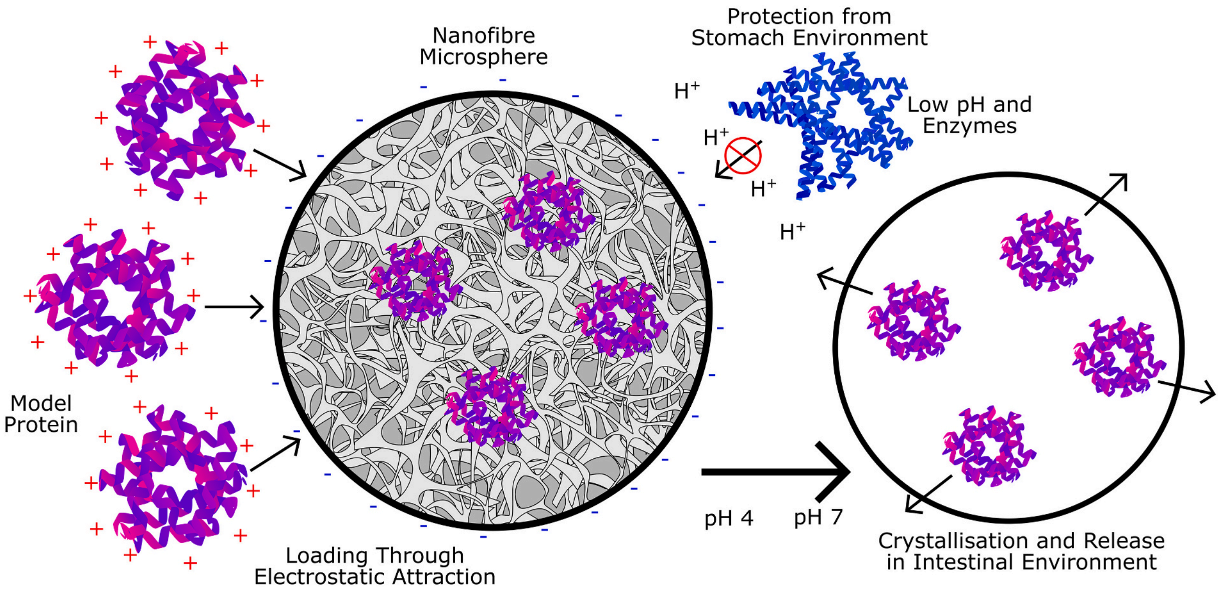

Fig. 8. Schematic of targeted enteric delivery. The delivered proteins, rendered cationic in the low pH loading conditions, diffuse into the core of the nanofibre microspheres, where they are bound electrostatically to the negatively charged pyrophosphate. The microsphere protects the proteins from the protease enzymes and acidic environment in the stomach, and when in the high pH of the intestine, crystallise and release the proteins.

networks, and then nanofibres that arrange into microspheres, and when agitated form nanotubes, before crystallising. This reaction represents the system transforming from the most kinetically favourable formation to the most thermodynamically stable, with the unit cell of the final mineral forming early in the prenucleation cluster, creating the nanoscale anisotropy that leads to the formation of the high aspect ratio intermediates. These intermediate phases, particularly the nanofibre microspheres, have a very large specific surface area, allowing for a high level of drug adsorption. Model proteins were adsorbed to the particles, which protected their payload in stomach conditions, before targeted release in the intestine.

Data availability statement

The raw/processed data required to reproduce these findings cannot be shared at this time as the data also forms part of an ongoing study.

CRediT authorship contribution statement

David Basset – Conceptualisation, Methodology, Formal Analysis, Investigation, Writing – Original Draft, Writing – Review and Editing.

Thomas Robinson - Writing – Original Draft, Writing – Review and Editing, Visualisation.

Reghan Hill – Methodology, Investigation.

Liam Grover - Conceptualisation, Methodology, Formal Analysis, Investigation, Writing – Original Draft, Writing – Review and Editing.

Jake Barralet Conceptualisation, Supervision, Project Administration, Funding Acquisition.

Declaration of competing interest

The authors declare that they have no known competing financial interests or personal relationships that could have appeared to influence the work reported in this paper.

Data availability

Data will be made available on request.

References

[1] A.A. Balhaddad, A.A. Kansara, D. Hidan, M.D. Weir, H.H.K. Xu, M.A.S. Melo, Toward dental caries: exploring nanoparticle-based platforms and calcium phosphate compounds for dental restorative materials, Bioact. Mater. 4 (2019) 43–55, https://doi.org/10.1016/J.BIOACTMAT.2018.12.002.

[2] N. Eliaz, N. Metoki, Calcium phosphate bioceramics: a review of their history, structure, properties, coating technologies and biomedical applications, Mater 10 (2017) 334, https://doi.org/10.3390/MA10040334, 2017, Vol. 10, Page 334.

[3] Jingyi Lu, Huijun Yu, Chuanzhong Chen, Biological properties of calcium phosphate biomaterials for bone repair: a review, RSC Adv. 8 (2018) 2015–2033, https://doi.org/10.1039/C7RA11278E.

[4] M.T. Islam, R.M. Felfel, E.A.A. Neel, D.M. Grant, I. Ahmed, K.M.Z. Hossain, Bioactive Calcium Phosphate–based Glasses and Ceramics and Their Biomedical Applications: A Review 8, 2017, https://doi.org/10.1177/2041731417719170 doi: 10.1177/2041731417719170.

[5] S.M. Londoño-Restrepo, R. Jeronimo-Cruz, B.M. Millán-Malo, E.M. Rivera-Muñoz, M.E. Rodriguez-García, Effect of the Nano crystal size on the X-ray diffraction patterns of biogenic hydroxyapatite from human, bovine, and porcine bones, Sci. Rep. 9 (2019) 1–12, https://doi.org/10.1038/s41598-019-42269-9.

[6] S. Ramesh, Z.Z. Loo, C.Y. Tan, W.J.K. Chew, Y.C. Ching, F. Tarlochan, H. Chandran, S. Krishnasamy, L.T. Bang, A.A.D. Sarhan, Characterization of biogenic hydroxyapatite derived from animal bones for biomedical applications, Ceram. Int. 44 (2018) 10525–10530, https://doi.org/10.1016/J.CERAMINT.2018.03.072.

[7] C.C. Ribeiro, C.C. Barrias, M.A. Barbosa, Preparation and characterisation of calcium-phosphate porous microspheres with a uniform size for biomedical applications, J. Mater. Sci. Mater. Med. 17 (2006) 455–463, https://doi.org/10.1007/s10856-006-8473-x.

[8] D.S. Seo, J.K. Lee, Dissolution of human teeth-derived hydroxyapatite, Ann. Biomed. Eng. 36 (2008) 132–140, https://doi.org/10.1007/s10439-007-9394-7.

[9] M.P. Ginebra, C. Canal, M. Espanol, D. Pastorino, E.B. Montufar, Calcium phosphate cements as drug delivery materials, Adv. Drug Deliv. Rev. 64 (2012) 1090–1110, https://doi.org/10.1016/j.addr.2012.01.008.

[10] Dan Huang, Bin He, Peng Mi, Calcium phosphate nanocarriers for drug delivery to tumors: imaging, therapy and theranostics, Biomater. Sci. 7 (2019) 3942–3960, https://doi.org/10.1039/C9BM00831D.

[11] T.V. Vasudevan, P. Somasundaran, C.L. Howie-Meyers, D.L. Elliott, K. P. Ananthapadmanabhan, Interaction of pyrophosphate with calcium phosphates, Langmuir 10 (1994) 320–325, https://doi.org/10.1021/la00013a047.

[12] M. Song, L. Dang, H. Wei, Evaluation of calcium binding capacity of chelating agents in calcium carbonate suspension and effects on calcium distribution of calcium chelating agents, Aust. J. Chem. 74 (2021) 557–563, https://doi.org/10.1071/CH20376.

[13] T.E. Robinson, E.A.B.B. Hughes, O.J. Wiseman, S.A. Stapley, S.C. Cox, L.M. Grover, Hexametaphosphate as a potential therapy for the dissolution and prevention of kidney stones, J. Mater. Chem. B 8 (2020) 5215–5224, https://doi.org/10.1039/d0tb00343c.

[14] T.E. Robinson, N.M. Eisenstein, S.C. Cox, R.J.A. Moakes, A.M. Thompson, Z. Ahmed, E.A.B. Hughes, L.J. Hill, S.A. Stapley, L.M. Grover, Local injection of a hexametaphosphate formulation reduces heterotopic ossification in vivo, Mater. Today Bio. 7 (2020), 100059, https://doi.org/10.1016/j.mtbio.2020.100059.

[15] M. Neufurth, X. Wang, S. Wang, R. Steffen, M. Ackermann, N.D. Haep, H. C. Schröder, W.E.G. Müller, 3D printing of hybrid biomaterials for bone tissue engineering: calcium-polyphosphate microparticles encapsulated by polycaprolactone, Acta Biomater. 64 (2017) 377–388, https://doi.org/10.1016/j.actbio.2017.09.031.

[16] A. Momeni, M.J. Filiaggi, Comprehensive study of the chelation and coacervation of alkaline earth metals in the presence of sodium polyphosphate solution, Langmuir 30 (2014) 5256–5266, https://doi.org/10.1021/la500474j.

[17] A. Dion, B. Berno, G. Hall, M.J. Filiaggi, The effect of processing on the structural characteristics of vancomycin-loaded amorphous calcium phosphate matrices, Biomaterials 26 (2005) 4486–4494, https://doi.org/10.1016/j.biomaterials.2004.11.010.

[18] T.V. Safronova, E.A. Mukhin, V.I. Putlyaev, A.V. Knotko, P.V. Evdokimov, T. B. Shatalova, Y.Y. Filippov, A.V. Sidorov, E.A. Karpushkin, Amorphous calcium phosphate powder synthesized from calcium acetate and polyphosphoric acid for bioceramics application, Ceram. Int. 43 (2017) 1310–1317, https://doi.org/10.1016/j.ceramint.2016.10.085.

[19] E.A.B.B. Hughes, T.E. Robinson, D.B. Bassett, S.C. Cox, L.M. Grover, Critical and diverse roles of phosphates in human bone formation, J. Mater. Chem. B 7 (2019) 7460–7470, https://doi.org/10.1039/c9tb02011j.

[20] C.J.S. Ibsen, H. Birkedal, Pyrophosphate-inhibition of apatite formation studied by in situ X-ray diffraction, Minerals 8 (2018) 65, https://doi.org/10.3390/min8020065.

[21] F. Grases, M. Ramis, A. Costa-Bauzá, Effects of phytate and pyrophosphate on brushite and hydroxyapatite crystallization: comparison with the action of other polyphosphates, Urol. Res. 28 (2000) 136–140, https://doi.org/10.1007/s002400050152.

[22] P. Gras, C. Rey, O. Marsan, S. Sarda, C. Combes, Synthesis and characterisation of hydrated calcium pyrophosphate phases of biological interest, Eur. J. Inorg. Chem. 2013 (2013) 5886–5895, https://doi.org/10.1002/ejic.201300955.

[23] P. Gras, S. Teychené, C. Rey, C. Charvillat, B. Biscans, S. Sarda, C. Combes, Crystallisation of a highly metastable hydrated calcium pyrophosphate phase, in: CrystEngComm, Royal Society of Chemistry, 2013, pp. 2294–2300, https://doi.org/10.1039/c2ce26499d.

[24] E.A. Zamora, R. Naik, Calcium Pyrophosphate Deposition Disease (CPDD). http://europepmc.org/books/NBK540151, 2019. (Accessed 10 September 2021).

[25] C. Kleiber Balderrama, A.K. Rosenthal, D. Lans, J.A. Singh, C.M. Bartels, Calcium pyrophosphate deposition disease and associated medical comorbidities: a National Cross-Sectional Study of US veterans, Arthritis Care Res. 69 (2017) 1400–1406, https://doi.org/10.1002/acr.23160.

[26] H.O. Alpar, S. Somavarapu, K.N. Atuah, V.W. Bramwell, Biodegradable mucoadhesive particulates for nasal and pulmonary antigen and DNA delivery, Adv. Drug Deliv. Rev. 57 (2005) 411–430, https://doi.org/10.1016/j.addr.2004.09.004.

[27] F. Wen, W. Zhang, G. Wei, Y. Wang, J. Zhang, M. Zhang, L. Shi, Synthesis of noble metal nanoparticles embedded in the shell layer of core-shell poly(styrene-co-4-vinylpyridine) micospheres and their application in catalysis, Chem. Mater. 20 (2008) 2144–2150, https://doi.org/10.1021/cm703378c.

[28] M.J. Beneš, D. Horák, F. Svec, Methacrylate-based chromatographic media, J. Sep. Sci. 28 (2005) 1855–1875, https://doi.org/10.1002/jssc.200500186.

[29] Y.E. Chang, D.Y. Youn, G. Ankonina, D.J. Yang, H.G. Kim, A. Rothschild, I.D. Kim, Fabrication and gas sensing properties of hollow SnO2 hemispheres, Chem. Commun. (2009) 4019–4021, https://doi.org/10.1039/b902542a.

[30] Z. Zhong, Y. Yin, B. Gates, Y. Xia, Preparation of mesoscale hollow spheres of TiO2 and SnO2 by templating against crystalline arrays of polystyrene beads, Adv. Mater. 12 (2000) 206–209, https://doi.org/10.1002/(SICI)1521-4095(200002)12:3<206::AID-ADMA206>3.0.CO;2-5.

[31] H.K. Kim, H.J. Chung, T.G. Park, Biodegradable polymeric microspheres with "open/closed" pores for sustained release of human growth hormone, J. Control. Release 112 (2006) 167–174, https://doi.org/10.1016/j.jconrel.2006.02.004.

[32] Y.-Y. Yang, T.-S. Chung, N.P. Ng, Morphology, drug distribution, and in vitro release profiles of biodegradable polymeric microspheres containing protein fabricated by double-emulsion solvent extraction/evaporation method, Biomaterials 22 (2001) 231–241, https://doi.org/10.1016/S0142-9612(00)00178-2.

[33] M. Remškar, Inorganic nanotubes, Adv. Mater. 16 (2004) 1497–1504, https://doi.org/10.1002/adma.200306428.

[34] M. Naeem, U.A. Awan, F. Subhan, J. Cao, S.P. Hlaing, J. Lee, E. Im, Y. Jung, J. W. Yoo, Advances in colon-targeted nano-drug delivery systems: challenges and solutions, Arch. Pharm. Res. 43 (2020) 153–169, https://doi.org/10.1007/s12272-020-01219-0.

[35] J. Richard, Challenges in oral peptide delivery: lessons learnt from the clinic and future prospects, Ther. Deliv. 8 (2017) 663–684, https://doi.org/10.4155/tde-2017-0024.

[36] S.H. Lee, R. Bajracharya, J.Y. Min, J.W. Han, B.J. Park, H.K. Han, Strategic approaches for colon targeted drug delivery: an overview of recent advancements, Pharmaceutics 12 (2020) 68, https://doi.org/10.3390/pharmaceutics12010068.

[37] M. Wikberg, J. Ulmius, G. Ragnarsson, Review article: targeted drug delivery in treatment of intestinal diseases, Aliment. Pharmacol. Ther. Suppl. 11 (1997) 109–115, https://doi.org/10.1111/J.1365-2036.1997.TB00815.X.

[38] P. Vass, B. Démuth, E. Hirsch, B. Nagy, S.K. Andersen, T. Vigh, G. Verreck, I. Csontos, Z.K. Nagy, G. Marosi, Drying technology strategies for colon-targeted oral delivery of biopharmaceuticals, J. Control. Release 296 (2019) 162–178, https://doi.org/10.1016/j.jconrel.2019.01.023.

[39] M.V. Ruby, A. Davis, R. Schoof, S. Eberle, C.M. Sellstone, Estimation of Lead and arsenic bioavailability using a physiologically based extraction test, Environ. Sci. Technol. 30 (1996) 422–430, https://doi.org/10.1021/es950057z.

[40] K. Ariga, Nanoarchitectonics: what's coming next after nanotechnology? Nanoscale Horiz. 6 (2021) 364–378, https://doi.org/10.1039/D0NH00680G.

[41] B.Q. Lu, N.A. Garcia, D.M. Chevrier, P. Zhang, P. Raiteri, J.D. Gale, D. Gebauer, Short-range structure of amorphous calcium hydrogen phosphate, Cryst. Growth Des. 19 (2019) 3030–3038, https://doi.org/10.1021/acs.cgd.9b00274.

[42] G. Mancardi, C.E. Hernandez Tamargo, D. Di Tommaso, N.H. de Leeuw, Detection of Posner's clusters during calcium phosphate nucleation: a molecular dynamics study, J. Mater. Chem. B 5 (2017) 7274–7284, https://doi.org/10.1039/C7TB01199G.

[43] I.G.R. Gutz, CurTiPot – pH and acid–base titration curves: analysis and simulation freeware, version 4.3.1. http://www.iq.usp.br/gutz/Curtipot_.htm, 2022.

[44] W.J.E.M. Habraken, J. Tao, L.J. Brylka, H. Friedrich, L. Bertinetti, A.S. Schenk, A. Verch, V. Dmitrovic, P.H.H. Bomans, P.M. Frederik, J. Laven, P. van der Schoot, B. Aichmayer, G. de With, J.J. DeYoreo, N.A.J.M. Sommerdijk, Ion-association complexes unite classical and non-classical theories for the biomimetic nucleation of calcium phosphate, Nat. Commun. 4 (2013) 1507.

[45] T. Balić-Žunić, M.R. Christoffersen, J. Christoffersen, Structure of the β form of calcium pyrophosphate tetrahydrate, Acta Crystallogr. Sect. B Struct. Sci. 56 (2000) 953–958, https://doi.org/10.1107/S0108768100009447.

[46] P.N. Nelson, A theoretical assessment of the primary hydration shell formation for calcium pyrophosphate, J. Mol. Struct. 1190 (2019) 144–147, https://doi.org/10.1016/j.molstruc.2019.04.077.

[47] E. Sayed, R. Haj-Ahmad, K. Ruparelia, M.S. Arshad, M.W. Chang, Z. Ahmad, Porous inorganic drug delivery systems—a review, AAPS PharmSciTech 18 (2017) 1507–1525, https://doi.org/10.1208/s12249-017-0740-2.

[48] M. Arruebo, Drug delivery from structured porous inorganic materials, Wiley Interdiscip. Rev. Nanomed. Nanobiotechnol. 4 (2012) 16–30, https://doi.org/10.1002/wnan.132.

[49] M.M. Dragosavac, G.T. Vladisavljević, R.G. Holdich, M.T. Stillwell, Production of porous silica microparticles by membrane emulsification, Langmuir 28 (2012) 134–143, https://doi.org/10.1021/la202974b.

[50] M. Lengyel, N. Kállai-Szabó, V. Antal, A.J. Laki, I. Antal, Microparticles, microspheres, and microcapsules for advanced drug delivery, Sci. Pharm. 87 (2019) 20, https://doi.org/10.3390/SCIPHARM87030020, 2019, Vol. 87, Page 20.

[51] V. Bansode, P. Gupta, N. Kateja, A.S. Rathore, Contribution of protein a step towards cost of goods for continuous production of monoclonal antibody therapeutics, J. Chem. Technol. Biotechnol. (2021), https://doi.org/10.1002/jctb.6686.

[52] J.L. Corchero, B. Gasser, D. Resina, W. Smith, E. Parrilli, F. Vázquez, I. Abasolo, M. Giuliani, J. Jäntti, P. Ferrer, M. Saloheimo, D. Mattanovich, S. Schwartz, M. L. Tutino, A. Villaverde, Unconventional microbial systems for the cost-efficient production of high-quality protein therapeutics, Biotechnol. Adv. 31 (2013) 140–153, https://doi.org/10.1016/j.biotechadv.2012.09.001.

[53] FDA, in: Food Additive Status List | FDA, U.S Food Drug Adm, 2019, pp. 1–95, doi: 10.1177/2041731417719170, https://www.fda.gov/food/food-additives-petitions/food-additive-status-list. (Accessed 17 March 2022).

[54] R. Greenwood, An electroacoustic investigation of concentrated aqueous suspensions of calcium pyrophosphate, Part. Part. Syst. Charact. 21 (2004) 415–418, https://doi.org/10.1002/ppsc.200400949.

[55] J. Puetz, F.M. Wurm, Recombinant proteins for industrial versus pharmaceutical purposes: a review of process and pricing, Processes. 7 (2019) 476, https://doi.org/10.3390/pr7080476.